J|A|C|S
ARTICLES

Published on Web 04/14/2010

Synthesis, Self-Assembly, Disassembly, and Reassembly of Two Types of Cu_2O Nanocrystals Unifaceted with {001} or {110} Planes

Ke Xin Yao,[†] Xiao Ming Yin,[‡] Tai Hong Wang,[‡] and Hua Chun Zeng*,[†]

Department of Chemical and Biomolecular Engineering, KAUST-NUS GCR Program, and Minerals, Metals, and Materials Technology Center, Faculty of Engineering, National University of Singapore, 10 Kent Ridge Crescent, Singapore 119260, and Key Laboratory for Micro-Nano Optoelectronic Devices of Ministry of Education and State Key Laboratory of Chemo/Biosensing and Chemometrics, Hunan University, Changsha 410082, P. R. China

Received January 7, 2010; E-mail: chezhc@nus.edu.sg

Abstract: In this work, we describe a solution-based synthesis of monodisperse Cu_2O nanocrystals with controllable sizes in the nanoscale regime. Two types of nanocrystals, cubes and rhombic dodecahedra unifaceted with either {001} or {110} crystal planes, have been prepared at a 100% morphological yield. In particular, synthetic parameters and formation processes of the Cu_2O nanocrystals have been investigated in detail, and a range of well-oriented supercrystals/superlattices built from the two types of nanobuilding blocks have been attained for the first time. It has been revealed that *n*-hexadecylamine used in the present work plays multiple roles: it serves as a chelating ligand to form $[Cu(NH_2C_{16}H_{33})_4]^{2+}$ complex precursor, as a phase-transferring agent to transfer divalent Cu^{2+} ions into the organic phase, as a reducing agent to generate monovalent Cu^+ (i.e., Cu_2O), as a passivating adsorbate to control crystal morphology, and as a surface capping agent to generate self-assemblies of nanocrystals via van der Waals interaction. Apart from synthesis and self-assembly, disassembly and reassembly of Cu_2O nanocrystals have also been investigated. The disassembly processes are accompanied with aggregative growths of nanocrystals, which can be attributed to a combined process of "oriented attachment" and Ostwald ripening, leading to permanent engagement and enlargement of nanocrystals. Finally, our self-assembled nanocrystals of Cu_2O show a lower detection limit, lower operating temperature, and higher sensitivity in ethanol vapor detection, compared with other Cu_2O-based alcohol sensors reported in the recent literature. A greater depletion layer of carrier and a relatively small contact potential may account for the observed sensing enhancement in the sensors made from the organized Cu_2O nanocrystals.

1. Introduction

Discrete nanostructured metals, metal oxides, and sulfides have a limited scope of applications due to their potential cytotoxicity and/or difficulties in separation and recovery after use. To develop these functional nanomaterials for practical applications, self-assembly and architectural aspects of their design and synthesis must be investigated, because the types of compositional and structural organization in the product materials will have significant impact on their ultimate performance. In this regard, self-assembly of nanoscale building blocks into one to three-dimensional (1D to 3D) organizations has attracted significant research interest over the past decade due to unique physicochemical properties of the organized materials and their emerging applications in many strategically important fields such as pharmaceuticals, consumer products, electronics, catalysis, energy and environmental protection, etc.[1−20] The investigated nanobuilding units for 1−3D architectures include simpler forms of nonuniform spherical nanoparticles, as well as more complex morphologies of nanocrystals and nanostructures with well-defined crystal size and facets or hierarchical branches and shelled configurations, etc. For instance, it has been revealed that photoluminescence spectra of faceted CdSe

---

[†] National University of Singapore.
[‡] Hunan University.

(1) Whitesides, G. M.; Grzybowski, B. *Science* **2002**, *295*, 2418–2421.
(2) Shenton, W.; Pum, D.; Sleytr, U. B.; Mann, S. *Nature* **1997**, *389*, 585–587.
(3) Li, M.; Schnablegger, H.; Mann, S. *Nature* **1999**, *402*, 393–395.
(4) Sun, S. H.; Murray, C. B.; Weller, D.; Folks, L.; Moser, A. *Science* **2000**, *287*, 1989–1992.
(5) Kim, F.; Kwan, S.; Akana, J.; Yang, P. D. *J. Am. Chem. Soc.* **2001**, *123*, 4360–4361.
(6) Puntes, V. F.; Krishnan, K. M.; Alivisatos, A. P. *Science* **2001**, *291*, 2115–2117.
(7) Velikov, K. P.; Christova, C. G.; Dullens, R. P. A.; van Blaaderen, A. *Science* **2002**, *296*, 106–109.
(8) Redl, F. X.; Cho, K. S.; Murray, C. B.; O'Brien, S. *Nature* **2003**, *423*, 968–971.
(9) Yu, D.; Wang, C. J.; Guyot-Sionnest, P. *Science* **2003**, *300*, 1277–1280.
(10) Dumestre, F.; Chaudret, B.; Amiens, C.; Renaud, P.; Fejes, P. *Science* **2004**, *303*, 821–823.
(11) Fan, H. Y.; Yang, K.; Boye, D. M.; Sigmon, T.; Malloy, K. J.; Xu, H. F.; Lopez, G. P.; Brinker, C. J. *Science* **2004**, *304*, 567–571.
(12) Wang, X.; Zhuang, J.; Peng, Q.; Li, Y. D. *Nature* **2005**, *437*, 121–124.
(13) Shevchenko, E. V.; Talapin, D. V.; Kotov, N. A.; O'Brien, S.; Murray, C. B. *Nature* **2006**, *439*, 55–59.
(14) Robinson, R. D.; Sadtler, B.; Demchenko, D. O.; Erdonmez, C. K.; Wang, L. W.; Alivisatos, A. P. *Science* **2007**, *317*, 355–358.

10.1021/ja100151f

superlattices have narrow-width symmetric shapes, compared with those of concentrated solutions and corresponding amorphous solids that have irregular asymmetric shapes.[18] The observed difference is attributed to energy transfer processes due to the size distribution and presence of nonuniform aggregates in concentrated solutions and amorphous solids and the absence of these factors in single-size nanocrystal superlattices.[18] Furthermore, it has also been reported that a considerably decreased fluorescence and a shortened fluorescence lifetime of CdSe nanocrystals can be observed in binary nanoparticle superlattices built of monodisperse CdSe and Au nanocrystals.[15] This observation indicates that energy is transferred from CdSe to surrounding Au nanocrystals and that the Au nanocrystals most probably also influence the radiative rate of the CdSe nanocrystals.[15]

The unique properties resulting from compositional and structural organizations have motivated chemists to develop solution-based synthetic methodologies for preparation of superstructures. As an example, apart from synthesis of common nanoparticles and nanocrystals, the emulsion method has also been used to fabricate 3D superstructures by a number of research groups.[21−23] In this prevailing approach, an oil phase containing nanoparticles is first dispersed in a water phase and stabilized by certain surfactants that interface the oil and water phases. After formation of a microemulsion in the water phase, the low-boiling organic solvent in the oil droplets is evaporated from the water phase by thermal treatment. Upon the removal of the organic solvent, condensation of nanoparticles (i.e., self-assembly process) is confined to the interior of an emulsion droplet or to a liquid−liquid interface. In another example, magnetic interaction between building units has been utilized in the self-assembly of nanoparticles.[24−27] Among the approaches to the formation of superstructures in literature, van der Waals, electrostatic, steric repulsion, and directional dipolar interactions have been frequently employed to obtain ordered functional superstructures.[4,8,13,15,28−30] The advantages of this approach are low-energy consumption, low cost, and simplicity of operational procedures compared with other methods. Moreover, this approach is applicable for a variety of nanoparticles such as metals, metal oxides/sulfides, and their mixtures.

In the field of synthesis and organization of transition metal oxides, cuprous oxide (cuprite Cu_2O) has attracted great attention in the latest years owing to its distinguished properties.[31−34] As a *p*-type semiconductor with a band gap energy of 2.17 eV and a large exciton binding energy of 140 meV, Cu_2O has shown a wide range of promising applications for chemical sensors,[31,35,36] all-oxide solar cells,[32] optical limiters,[33] photocatalysis,[34] and CO oxidation.[37] In exploiting its outstanding properties, Cu_2O has been prepared into various product morphologies, including nanoparticles,[38,39] nanocubes,[34,40−42] nanocages,[43,44] nanowires,[45,46] solid and hollow spheres,[31,33,35,47,48] and polyhedrons.[49−52] Although great progress has been made in the general synthesis of Cu_2O nanomaterials, size, and morphological control for monodisperse Cu_2O building blocks still remains as a challenging subject of research. Up to now, there has been no report on long-range ordered organizations of this important functional material into supercrystals and superlattices, because of difficulties in preparation of equally sized nanocrystals in a spatial scale of small than 100 nm and/or generation of appropriate intercrystal connectivity for product architectures.

This contribution is therefore focused on development of synthetic methods for Cu_2O nanocrystals with precise control over crystal size and morphological uniformity. More importantly, self-assembly, disassembly, and reassembly of as-prepared Cu_2O nanocrystals have been investigated with respect to their various structural architectures and potential applications.

---

(15) Shevchenko, E. V.; Ringler, M.; Schwemer, A.; Talapin, D. V.; Klar, T. A.; Rogach, A. L.; Feldmann, J.; Alivisatos, A. P. *J. Am. Chem. Soc.* **2008**, *130*, 3274–3275.

(16) Tao, A. R.; Huang, J. X.; Yang, P. D. *Acc. Chem. Res.* **2008**, *41*, 1662–1673.

(17) Huo, Z. Y.; Tsung, C. K.; Huang, W. Y.; Fardy, M.; Yan, R. X.; Zhang, X. F.; Li, Y. D.; Yang, P. D. *Nano Lett.* **2009**, *9*, 1260–1264.

(18) Zaitseva, N.; Dai, Z. R.; Leon, F. R.; Krol, D. *J. Am. Chem. Soc.* **2005**, *127*, 10221–10226.

(19) Murray, C. B.; Kagan, C. R.; Bawendi, M. G. *Science* **1995**, *270*, 1335–1338.

(20) Freeman, R. G.; Grabar, K. C.; Allison, K. J.; Bright, R. M.; Davis, J. A.; Guthrie, A. P.; Hommer, M. B.; Jackson, M. A.; Smith, P. C.; Walter, D. G.; Natan, M. J. *Science* **1995**, *267*, 1629–1632.

(21) Bai, F.; Wang, D. S.; Huo, Z. Y.; Chen, W.; Liu, L. P.; Liang, X.; Chen, C.; Wang, X.; Peng, Q.; Li, Y. D. *Angew. Chem., Int. Ed.* **2007**, *46*, 6650–6653.

(22) Wang, D.; Xie, T.; Peng, Q.; Li, Y. *J. Am. Chem. Soc.* **2008**, *130*, 4016–4022.

(23) Zhuang, J. Q.; Wu, H. M.; Yang, Y. G.; Cao, Y. C. *Angew. Chem., Int. Ed.* **2008**, *47*, 2208–2212.

(24) Erb, R. M.; Son, H. S.; Samanta, B.; Rotello, V. M.; Yellen, B. B. *Nature* **2009**, *457*, 999–1002.

(25) Guo, L.; Liang, F.; Wen, X. G.; Yang, S. H.; He, L.; Zheng, W. Z.; Chen, C. P.; Zhong, Q. P. *Adv. Funct. Mater.* **2007**, *17*, 425–430.

(26) Tsang, S. C.; Yu, C. H.; Tang, H. L.; He, H.; Castelletto, V.; Hamley, I. W.; Narayanan, T.; Lo, C. C. H.; Tam, K. *Chem. Mater.* **2008**, *20*, 4554–4556.

(27) Gao, J. H.; Zhang, B.; Zhang, X. X.; Xu, B. *Angew. Chem., Int. Ed.* **2006**, *45*, 1220–1223.

(28) Lu, W.; Fang, J.; Stokes, K. L.; Lin, J. *J. Am. Chem. Soc.* **2004**, *126*, 11798–11799.

(29) Lu, W.; Liu, Q.; Sun, Z.; He, J.; Ezeolu, C.; Fang, J. *J. Am. Chem. Soc.* **2008**, *130*, 6983–6991.

(30) Yang, S. W.; Gao, L. *J. Am. Chem. Soc.* **2006**, *128*, 9330–9331.

(31) Zhang, J. T.; Liu, J. F.; Peng, Q.; Wang, X.; Li, Y. D. *Chem. Mater.* **2006**, *18*, 867–871.

(32) Yuhas, B. D.; Yang, P. D. *J. Am. Chem. Soc.* **2009**, *131*, 3756–3761.

(33) Gao, J. N.; Li, Q. S.; Zhao, H. B.; Li, L. S.; Liu, C. L.; Gong, Q. H.; Qi, L. M. *Chem. Mater.* **2008**, *20*, 6263–6269.

(34) (a) Kuo, C. H.; Chen, C. H.; Huang, M. H. *Adv. Funct. Mater.* **2007**, *17*, 3773–3780. (b) Kuo, C.-H.; Huang, M. H. *J. Phys. Chem. C* **2008**, *112*, 18355–18360. (c) Ho, J.-Y.; Huang, M. H. *J. Phys. Chem. C* **2009**, *113*, 14159–14164.

(35) Zhang, H. G.; Zhu, Q. S.; Zhang, Y.; Wang, Y.; Zhao, L.; Yu, B. *Adv. Funct. Mater.* **2007**, *17*, 2766–2771.

(36) Liu, J.; Wang, S. Z.; Wang, Q.; Geng, B. Y. *Sens. Actuators, B* **2009**, *143*, 253–260.

(37) White, B.; Yin, M.; Hall, A.; Le, D.; Stolbov, S.; Rahman, T.; Turro, N.; O'Brien, S. *Nano Lett.* **2006**, *6*, 2095–2098.

(38) Yin, M.; Wu, C. K.; Lou, Y. B.; Burda, C.; Koberstein, J. T.; Zhu, Y. M.; O'Brien, S. *J. Am. Chem. Soc.* **2005**, *127*, 9506–9511.

(39) Son, S. U.; Park, I. K.; Park, J.; Hyeon, T. *Chem. Commun.* **2004**, 778–779.

(40) Gou, L.; Murphy, C. J. *Nano Lett.* **2003**, *3*, 231–234.

(41) Park, J. C.; Kim, J.; Kwon, H.; Song, H. *Adv. Mater.* **2009**, *21*, 803–807.

(42) Teo, J. J.; Chang, Y.; Zeng, H. C. *Langmuir* **2006**, *22*, 7369–7377.

(43) Lu, C. H.; Qi, L. M.; Yang, J. H.; Wang, X. Y.; Zhang, D. Y.; Xie, J. L.; Ma, J. M. *Adv. Mater.* **2005**, *17*, 2562–2567.

(44) Kuo, C.-H.; Huang, M. H. *J. Am. Chem. Soc.* **2008**, *130*, 12815–12820.

(45) Tan, Y.; Xue, X.; Peng, Q.; Zhao, H.; Wang, T.; Li, Y. *Nano Lett.* **2007**, *7*, 3723–3728.

(46) Wang, W. Z.; Wang, G. H.; Wang, X. S.; Zhan, Y. J.; Liu, Y. K.; Zheng, C. L. *Adv. Mater.* **2002**, *14*, 67–69.

(47) Xu, H. L.; Wang, W. Z. *Angew. Chem., Int. Ed.* **2007**, *46*, 1489–1492.

(48) Chang, Y.; Teo, J. J.; Zeng, H. C. *Langmuir* **2005**, *21*, 1074–1079.

(49) Siegfried, M. J.; Choi, K. S. *Angew. Chem., Int. Ed.* **2005**, *44*, 3218–3223.

(50) Siegfried, M. J.; Choi, K. S. *Adv. Mater.* **2004**, *16*, 1743–1746.

(51) Siegfried, M. J.; Choi, K. S. *J. Am. Chem. Soc.* **2006**, *128*, 10356–10357.

(52) Chang, Y.; Zeng, H. C. *Cryst. Growth Des.* **2004**, *4*, 273–278.

A range of supercrystals and superlattices with well-defined crystal orientations has been assembled from two types of monodisperse crystal building blocks of Cu_2O for the first time. On the basis of our synthetic and analytical results, we have further identified several process parameters and addressed mechanistic issues related to the preparative and organizing processes of Cu_2O nanocrystals. Using our orderly organized Cu_2O as a sensing material, we have also demonstrated a significant improvement for ethanol sensing, compared with reported works in the recent literature.

2. Experimental Section

2.1. Synthesis and Self-Assembly of Cu_2O Superlattices. In this work, nanostructured cuprous oxide was obtained via refluxing copper(II) acetate solution under elevated temperatures. In a typical experiment, a given amount of 1-hexadecylamine (HDA, $NH_2C_{16}H_{33}$, 90%, Fluka) was heated to 60 °C and kept for a while until HDA completely transformed into transparent liquid. Two methods were used for preparations of Cu_2O nanocrystals: (i) For synthesis of Cu_2O nanocubes, 0.10−0.80 g of copper(II) acetate monohydrate ($C_4H_8CuO_5$ or $Cu(Ac)_2 \cdot H_2O$, 99%, Fluka) and 20 mL of the above warm HDA were added into a 100-mL flask. (ii) For synthesis of Cu_2O dodecahedra, 0.10−0.80 g of copper(II) acetate monohydrate, 1.0−10.0 mL of the warm HDA, and 10.0−20.0 mL of undecane ($C_{11}H_{24}$, 99%, SAFC) were added into a 100-mL flask. The above mixtures were preheated to 90 °C and kept for 10 min under vigorous stirring to ensure the complete dissolution of copper acetate into solution, followed by a rapid temperature increase to 160−220 °C (mostly 200 °C), where they were kept for 15−90 min. The products were then centrifuged (3500 rpm, 3 min) and rinsed several times with ethanol in order to remove the residual reactants. Finally, the precipitates were dried in a vacuum oven at 60 °C for 4 h.

2.2. Disassembly and Reassembly of Cu_2O Superlattices. A 10 mg/mL Cu_2O suspension was prepared by dispersing 100 mg of fresh Cu_2O sample into 10 mL of toluene (99.9%, Fisher) under stirring. Then 0.2−5.0 mL of the above solution was added into 50 mL of toluene, followed by refluxing at 120 °C (oil bath temperature) for 15−120 min. After the refluxing, disassembled Cu_2O suspension was concentrated to 0.5−1.0 mg/mL for reassembly by vacuum evaporation at 60 °C and 500 mbar. In some cases, reassembly of the above disassembled Cu_2O nanocrystals was carried out on TEM sample grids at room temperature. In this type of reassembling processes, a 200 mesh copper grid coated with Formvar/carbon was place at the bottom of 5-mL sample vials, followed by injecting 50 μL of the above reflux treated Cu_2O suspension into the vials. Afterward, the sample vials stood overnight at room temperature to allow a slow evaporation of the solvent and reorganization of nanocrystals.

2.3. Gas Sensor Application for Ethanol Detection. A fixed amount (1.0 mg) of each investigated Cu_2O sample was mixed with ethanol and hand-ground in an agate mortar for 30 min in order to form a slurry. Afterward the slurry was pasted uniformly on the external surface of the ceramic tubes of the sensors. After being dried at room temperature, the sensors were annealed at 200 °C for 2 h in a tube furnace under a nitrogen atmosphere. Subsequently, the prepared sensors were connected in series with a standard resistor and aged for 24 h with a heating voltage of 4 V. Under an applied dc voltage of 5 V, the voltage across the standard resistor was measured to evaluate the electrical resistance of the sensors. Gas sensing tests were carried out in a commercial gas sensing measurement system at a relative humidity of 50%. The resistance was recorded after putting the sensors at a working temperature of 150 °C into the gas chamber, which was charged with ethanol vapor (target analyte) at different concentrations.[53] The sensitivity (S) of the sensors was also computed according to $S = R_G/R_A$, where R_G and R_A are the resistances of the sensor in presence or in absence of analyte gas when the sensor is under operating conditions.

2.4. Materials Characterization. XRD Measurement. The crystallographic information of the as-prepared samples was investigated by powder X-ray diffraction (XRD). The XRD patterns with diffraction intensity versus 2θ were recorded in a Shimadzu X-ray diffractometer (model 6000) with Cu Kα radiation (λ = 1.5406 Å) from 25 to 80° at a scanning speed of 2°/min. X-ray tube voltage and current were set at 40 kV and 30 mA, respectively, in the measurements.

TEM/HRTEM/SAED Measurement. Investigations with high-resolution analytical transmission electron microscopy (TEM and HRTEM) and selected area electron diffraction (SAED) were carried on a JEM-2010 and a JEM-2100F with an electron kinetic energy of 200 kV. Unless otherwise stated, the specimens for TEM imaging were prepared by dispersing solid samples in toluene. Briefly, 2−3 drops of this well-dispersed suspension was dropped onto a carbon-coated 200-mesh copper grid, followed by drying of the sample under ambient condition before it was placed in the sample holder of the microscope.

XPS Measurement. X-ray photoelectron spectroscopy (XPS) investigation was conducted in an AXIS-HSi spectrometer (Kratos Analytical) using a monochromated Al Kα X-ray source (1486.6 eV). The as-prepared samples were mounted onto the double-sided adhesive tape on the sample stubs. The XPS spectra of the studied elements were measured with a constant analyzer pass energy of 40.0 eV. All binding energies (BEs) were referred to the C 1s peak (284.6 eV) arising from surface hydrocarbons (or adventitious hydrocarbon).

FTIR Spectroscopic Measurement. Chemical bonding information on both the surfactant and Cu_2O nanocrystals was studied with Fourier transform infrared spectroscopy (FTIR, Bio-Rad) using the potassium bromide (KBr) pellet technique. In making the KBr pellets, about 1 mg of precipitated Cu_2O powder was diluted with approximately 100 mg of KBr powder. Each FTIR spectrum was collected after 16 scans with a resolution of 4 cm^{-1} between 400 and 4000 cm^{-1}.

TGA Measurement. The thermal behavior of the as-prepared Cu_2O products was characterized with thermogravimetric analysis (TGA) in a TA Instruments TGA-2050. In each experiment, about 10 mg of the sample was heated at a rate of 10 °C/min from 30 to 900 °C with a flowing nitrogen gas stream at 100 mL/min.

UV−vis Spectroscopic Analysis. UV absorption spectra of some divalent copper complexes discussed in this work were measured on a UV−vis scanning spectrophotometer (Shimadzu UV-2450). A small amount of sample (1−5 mg of dry Cu^{2+}-HDA solid or copper(II) acetate monohydrate ($Cu(Ac)_2 \cdot H_2O$)) was first dissolved in ethanol solvent with assistance of sonication in an ultrasonic water bath in order to obtain Cu^{2+}-HDA complex and $Cu(Ac)_2 \cdot H_2O$ solutions for this UV−vis study. For the formation of Cu^{2+}-NH_3 complex, a certain amount of ammonia solution was further added into the $Cu(Ac)_2 \cdot H_2O$ solution, while keeping Cu^{2+}/NH_3 molar ratio at 1:5. The above solutions were then transferred respectively into a 1-cm path quartz cuvette for measurement, using pure ethanol as a reference.

3. Results and Discussion

3.1. Nanobuilding Blocks and Superlattice Structures. Two types of Cu_2O nanobuilding blocks in a 100% morphological yield were prepared with our current synthetic routes. One unique structural feature should be noted is that both types of building units are unifaceted with only one family of surfaces, either {001} or {110}, as illustrated in Figure 1. Some representative XRD patterns of as-synthesized Cu_2O nanocubes and dodecahedra upon reaction time are displayed in Figure

---

(53) Li, C. C.; Yin, X. M.; Wang, T. H.; Zeng, H. C. *Chem. Mater.* **2009**, *21*, 4984–4992.

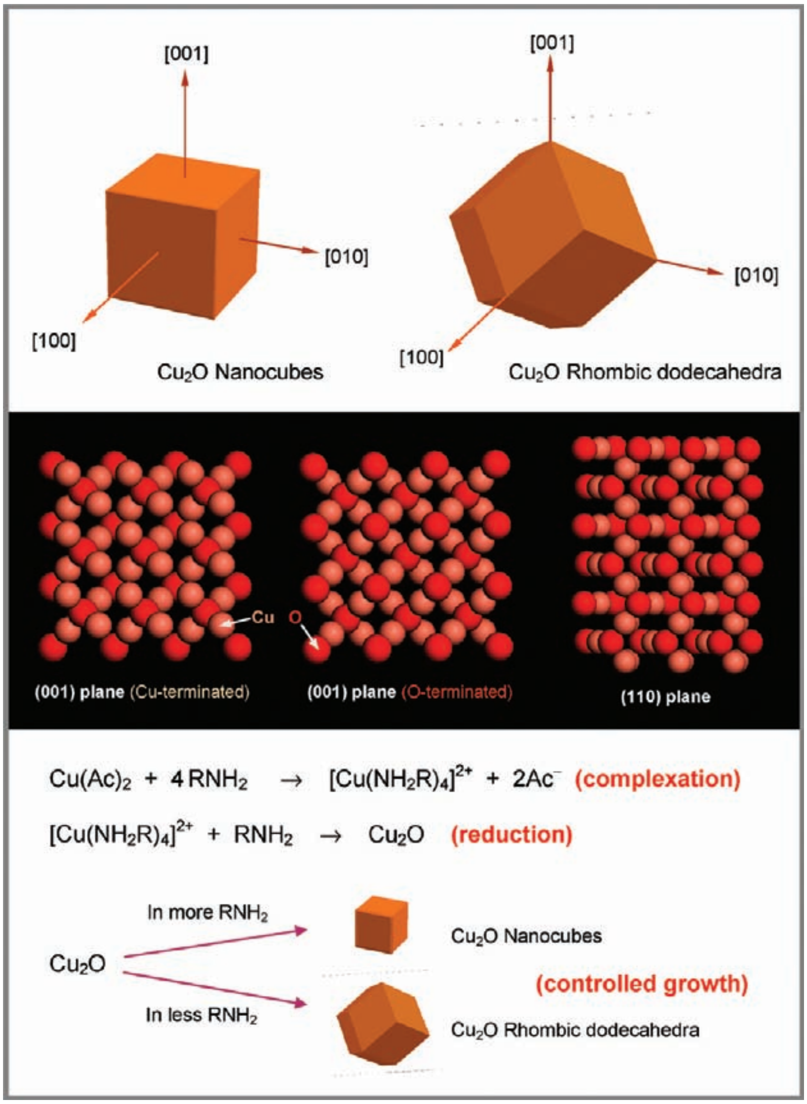

$$Cu(Ac)_2 + 4RNH_2 \rightarrow [Cu(NH_2R)_4]^{2+} + 2Ac^- \quad \text{(complexation)}$$

$$[Cu(NH_2R)_4]^{2+} + RNH_2 \rightarrow Cu_2O \quad \text{(reduction)}$$

Figure 1. Structural illustration of two different types of Cu_2O nanobuilding blocks (nanocubes and rhombic dodecahedra) investigated in the current work (upper panel), crystallographic structures of (001) and (110) planes of Cu_2O (middle panel) and main process steps and the multiple roles of alkylamines in the controlled synthesis of Cu_2O nanocrystals (lower panel).

2a, and the diffraction patterns (nanocubes (1 h) and dodecahedra (0.5 h)) can be assigned perfectly to the cubic crystal system of cuprite Cu_2O (JCPDS card no. 03-0892; space group $Pn\bar{3}m$; lattice constant $a_o = 4.26$ Å). The compositional analysis with EDX technique also affirms that the atomic ratio of Cu to O is indeed close to 2:1 in these Cu_2O samples (e.g., Figure 2b). Consistent with the high crystallinity revealed by XRD, our HRTEM investigation indicates that the Cu_2O nanocubes are single-crystalline. In particular, lattice fringes of d_{110}, d_{200}, and d_{020} can be clearly resolved in the HRTEM image of Figure 2c. Similar to the nanocubes, Cu_2O rhombic dodecahedra are also single crystals, and their lattice fringes of d_{200}, d_{111}, and d_{220} can be seen in the image of Figure 2d. It should be mentioned that although polydisperse microcrsytals of Cu_2O rhombic dodecahedra have been reported very recently,[54] our present synthetic approach can successfully produce uniform Cu_2O rhombic dodecahedra down to a nanoscale range of only 20−70 nm. Because these crystal building blocks are highly monodisperse, we are now able to organize them into various novel superlattices that have not been reported before.

Owing to the well-faceted crystal planes and presence of surfactant molecules (HDA) on the external surfaces of the above two types of nanocrystals, a series of self-assembled supercrystals and superlattices has been realized in the present work. The first type of building blocks, the Cu_2O nanocubes, which are terminated with six crystal planes of {100}, {010}, and {001} (Figure 1), can be organized into supercrystals with a simple cubic crystal system. In Figure 3, we present some representative TEM images of these supercrystals. Although the central region of cubic aggregates is too dark to observe, the cubic superlattice structures (Figure 3a) can be easily identified by tilting the observed sample with a certain angle (Figure 3b). In the cubic crystal system, a crystal building unit has five and six nearest neighboring units in the surface and bulk phases, respectively (color inset, Figure 3a). As listed in Table 1, likewise for the monolayer (2D) array each Cu_2O cube has four nearest neighboring cubes, whereas for the multilayer (3D) assemblage each Cu_2O cube can use all its surface planes to generate self-assembly with six nearest neighboring ones. The

---

(54) Liang, X. D.; Gao, L.; Yang, S. W.; Sun, J. *Adv. Mater.* **2009**, *21*, 2068–2071.

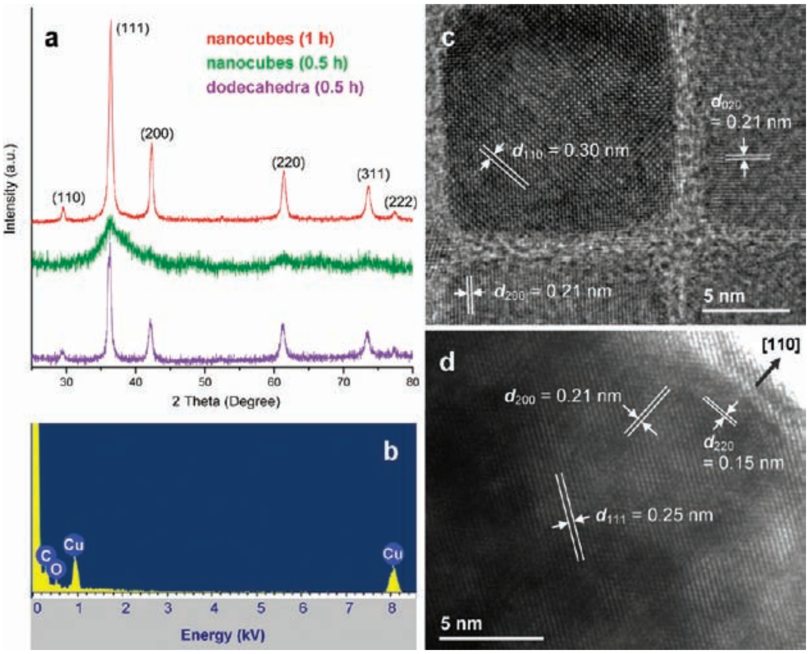

Figure 2. Structural and compositional characterization of Cu_2O nanobuilding blocks: (a) XRD patterns of nanocubes (after 0.5 and 1.0 h of reaction) and dodecahedra (after 0.5 h of reaction), (b) a representative EDX spectrum of nanocubes, (c) HRTEM image of nanocubes, and (d) HRTEM image of a dodecahedron.

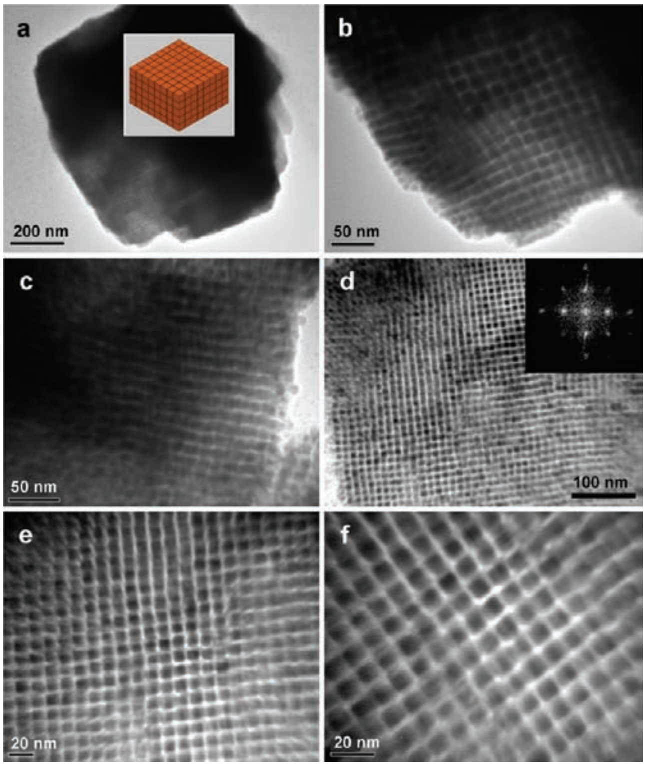

Figure 3. Self-assemblies of Cu_2O nanocubes (TEM images): (a) a supercrystal composed of cubic arrangement of nanocubes, (b) detailed view on the supercrystal (bottom area) in panel a, (c) edge and intercrystal gap of supercrystals, (d) a thin supercrystal and its FFT pattern (inset), and (e and f) detailed views on the cubic assemblies in supercrystals (superlattices) at different magnifications. Color inset illustrates the cubic arrangement of nanocubes in the supercrystals.

as-prepared Cu_2O nanocubes have a uniform shape and a narrow size distribution of 9.1 ± 0.6 nm. Under a higher magnification, it is found that their intercube distance is equally spaced and the average distance between cubic crystals is around 1.9 nm (Figure 2c). According to the formula L (nm) $= 0.25 + 0.127n$ (in which n is the number of carbon atoms in the alkyl chain), the estimated length of $C_{16}NH_2$ should be around 2.28 nm.[55] Compared with the actual distance of 1.9 nm observed between nanocubes, HDA molecules on the Cu_2O surfaces must have adopted a tilting configuration and/or must interpenetrate each other. The fast Fourier transform (FFT) patterns for some thinner 3D arrays also demonstrate the highly ordered stacking of the nanocubes (Figure 3d). From our HRTEM images (Figure 2c), we can find that nanocubes are indeed terminated by (100), (−100), (010), (0−10), (001) and (00−1) facets with high crystallinity. In all of these assemblages, square surface unit cell and simple cubic unit cell can be used to describe the observed 2D (i.e., surface) and 3D (i.e., bulk) superlattices. Quite interestingly, the surfaces of these Cu_2O supercrystals are also bordered with "crystal planes" of the {001} family, where individual surface nanocubes have five nearest neighbors, resembling the atomic or molecular species in the normal cubic crystal counterparts.

Unlike the simple cubic building blocks, the rhombic dodecahedral building blocks of Cu_2O can produce a much richer variety of assembled structures due to their more complex geometrical features, as summarized in Table 1 and Figures 4−7. In all of these artificial structures, the specific crystallographic orientation of an overall crystal assemblage depends critically on an initial aggregative "nucleation" of building blocks on the TEM sample grid (i.e., support for the Cu_2O crystals). While it would prefer to have a maximum contact with the support underneath, a rhombic dodecahedral crystal should also have a maximum engagement with its neighboring building crystals at the same time. In Figure 4 (also refer to Table 1), the [112]-oriented assemblies of rhombic dodecahedra are displayed. The building blocks of Cu_2O in the first layer use one of their 24 edges to stand perpendicularly along the [112] axis of the crystal.

---

(55) Du, W. M.; Qian, X. F.; Ma, X. D.; Gong, Q.; Cao, H. L.; Yin, H. *Chem.*−*Eur. J.* **2007**, *13*, 3241–3247.

Table 1. Summery of Cu_2O Superlattices Studied in This Work

building unit	assembly orientation	neighboring contact facets	contact with substrate	no. of contacting facets in 2D superlattices	no. of contacting facets in 3D superlattices[a]
cubes	[001]	{100}	plane	4	6
dodecahedra	[112]	{110}	line	6	12
dodecahedra	[111]	{110}	point	6	12
dodecahedra	[001]	{110}	point	4	12
dodecahedra	[011]	{110}	plane	2	4

[a] For cube building blocks, there is only one type of 3D packing in superlattices: simple cubic structure. Although four different assembled structures of rhombic dodecahedra have been identified above, there are actually only two types of packing arrangements (12 or 4 contacting facets in 3D superlattices). In all of the cases, every rhombic facet of a rhombic dodecahedron can make contacts with neighboring rhombic faces of adjacent rhombic dodecahedra. The dodecahedral building blocks form 2D and then 3D extended structures as the solvent evaporates. Because there are several different ways of 2D extended structures these dodecahedral building blocks can form, different packing orientations with respect to the plane of the underlying substrate can be obtained when the assembled structures finally deposit on the substrate surface (e.g., TEM sample grids).

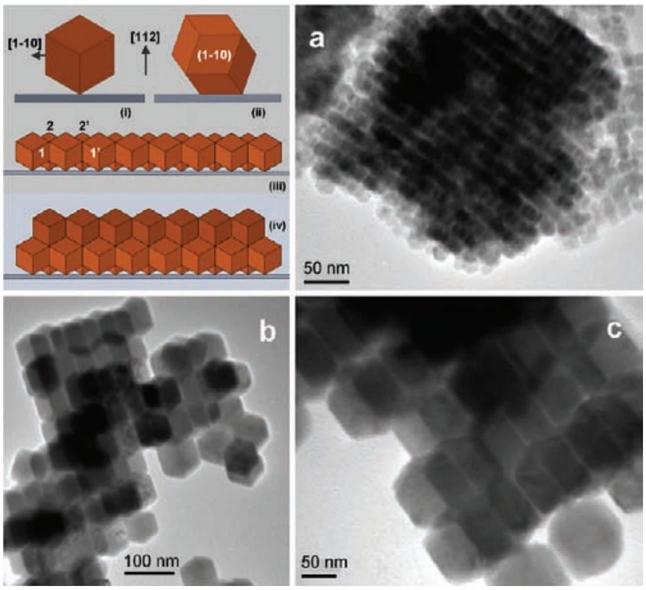

Figure 4. [112]-Oriented assemblies of Cu_2O rhombic dodecahedra at different magnifications (a−c, TEM images). Color inset illustrates (i) front view and (ii) side view of a Cu_2O dodecahedron standing perpendicularly (i.e., along the [112] axis of Cu_2O) on one of its 24 edges, (iii) single-layered arrangement, and (iv) double-layered arrangement in the superlattices.

Along an assembling line of the [1−10] direction, a rhombic dodecahedron can use two of its crystal planes to generate maximum contact (contact area is 100%; color inset (iii)) with two dodecahedra in each side (marked as 1 and 1′). Four other neighboring dodecahedra [two on the front (not shown) and two on the back (marked as 2 and 2′)] can also be in contact with this dodecahedron, but the contact area between two rhombic planes decreases to 50% with this type of geometric arrangements (color insets (iii) and (iv)). However, 100% contact of crystal planes for all building crystal units can still be attained when the dodecahedra in the alternate rows lose their contacts with the support, that is, the row behind rises in order to have a plane-to-plane overlap with the front row. The assembly process can be continued in a similar fashion for the second (Figure 4c) as well as consecutive layers, and overall 3D assemblages can thus be obtained (Figure 4a,b). In addition to the edge contact with the support, the rhombic dodecahedra of Cu_2O can also stand on their corners while generating self-assembled structures. In such organizations, the assembling connectivity predominantly comes from a collective crystal plane contact among the neighboring ones. Two types of such organizations have been revealed in our Cu_2O rhombic dodecahedral samples. The first type is shown in Figure 5, where a rhombic dodecahedron stands along the [111] axis of crystal while all of its six rhombic crystal planes along the [1−10], [10−1], [01−1], [−110], [−101] and [0−11] directions are connecting with its neighboring crystal units. Because this point-standing is rather unstable and relies largely on a mutual engagement among the participating dodecahedral crystals, some crystals cannot stand steadily, especially those in the boundary regions where the [10−1]-oriented crystal units can be found (Figure 5a). The second type of point-standing arrangement is presented in Figure 6, where the rhombic dodecahedra are standing on their sharp tips formed from four crystal planes (10−1), (01−1), (−10−1) and (0−1−1). In the [001]-oriented 2D-array, each dodecahedron can only have four immediate adjacent units, although it also has 12 neighboring units in the 3D aggregates (Table 1). Similar to the [111]-oriented superlattices, it is difficult to keep all of the rhombic dodecahedra in a standing position along the [001], and some [110]-oriented crystals can also be found in the boundary regions (Figure 6c). The 2D expansion of these square arrays is thus hampered by the difficulty in generating initial mutual engagement, and the size of this type of assemblages is normally small, including their 3D superlattices. From the above assembling cases, one may wonder why the rhombic dodecahedra of Cu_2O do not simply land on their flat {011} planes (i.e., (011) and (0−1−1)) and generate respective 2D or 3D superlattices. In fact, when a rhombic dodecahedron lands on the support with one of these two crystal planes, there are only two crystal planes (i.e., (01−1) and (0−11); they are shown as sharper edges in the TEM image contrasts of Figure 7) that are parallel to the [011] direction and can give rise to the planar contact with other crystal units. Apparently, this 1D lined assembly is relatively easier, in comparison with 2D or 3D assemblies. Nonetheless, weak engagement among these 1D chains can also be attained by using their four edges (shown as blur contrasts in the TEM images) to form 2D arrays, which is shown in Figure 7a (see color inset (v)), although in some cases they can also use their shoulder crystal planes to generate contacts between two neighboring rows (Figure 7b). It should also be mentioned that it is difficult to have crystallographically perfect long-ranged 1D alignment, because of presence of defects. For example, misoriented crystal units cause distortion of the arrays, which limits commensurate horizontal expansion (Figure 7c,d), and assembly of multilayer superlattices using these crystal building blocks is also hindered due to the difficulty in obtaining unioriented 2D arrays (color inset (v)). Nonetheless, a simple pile-up of these randomly oriented crystals can also give rise to 3D assemblages in which the crystal units are stacked one another along the [011] direction with their flat {011} crystal planes (Figure 7e).

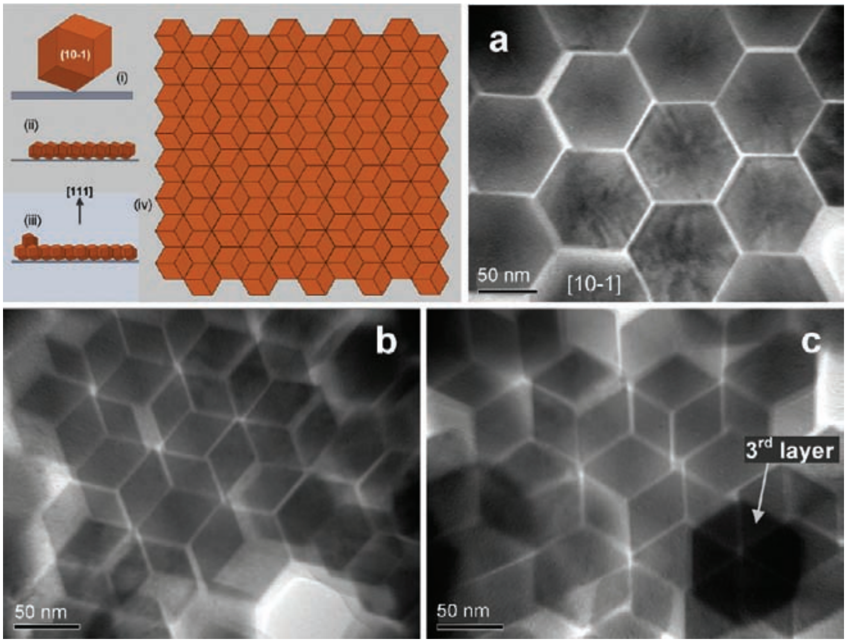

Figure 5. [111]-Oriented assemblies of Cu_2O rhombic dodecahedra (TEM images): (a) single layer array, (b) double layer arrangement, and (c) a dodecahedron standing on a double-layered structure. Color inset illustrates (i) a dodecahedron standing along the [111] axis of Cu_2O (viewed along the [10−1] axis), (ii) side view of a monolayer array, (iii) a dodecahedron standing on a monolayer array, and (iv) top view of a monolayer array (viewed along the [111] axis).

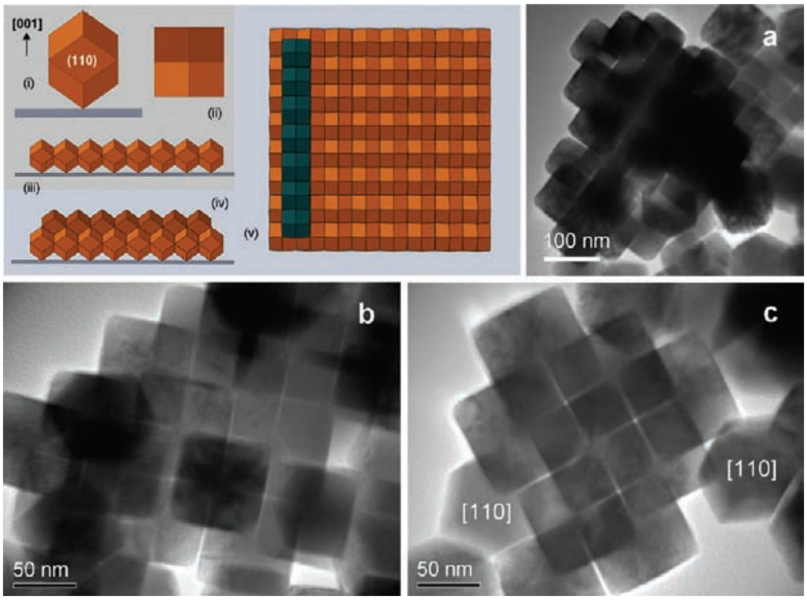

Figure 6. [001]-Oriented assemblies of Cu_2O rhombic dodecahedra (a−c, TEM images) viewed along the [001] axis of the crystal at different magnifications. Color inset illustrates (i) side view and (ii) top view of a Cu_2O dodecahedron standing along the [001] axis, (iii) side view of a monolayer array, (iv) side view of a double-layered arrangement, and (v) top view of a monolayer array and a row of dodecahedra (dark green) in the second layer.

3.2. Formation and Synthetic Parameters of Nanobuilding Blocks. Apart from the above geometrical investigation on the nanocrystals assemblies, we have further examined a range of synthetic parameters such as temperature and concentration, etc., in order to have an understanding on the formation and self-assembly of Cu_2O nanocrystals. In particular, we find that 1-hexadecylamine (HDA) molecules play multiple roles in the present approach. First of all, a divalent copper complex with HDA ligands, Cu^{2+}-HDA (i.e., $[Cu(NH_2C_{16}H_{33})_4]^{2+}$), was prepared as a copper precursor by mixing copper(II) acetate monohydrate ($Cu(Ac)_2 \cdot H_2O$) and HDA ($NH_2C_{16}H_{33}$) at 90 °C. After the mixture was stirred for several minutes, the colorless transparent HDA turned a bright blue color, indicating formation of Cu^{2+}-HDA complex whose UV-absorption spectrum is similar to that of the well-known $[Cu(NH_3)_4]^{2+}$, as compared in Figure 8a.[56] After this complexational conversion, Cu^{2+} ions from $Cu(Ac)_2 \cdot H_2O$ can be gradually transferred into nonpolar solvents (e.g., HDA, which was also a solvent used in the present case) in the form of Cu^{2+}-HDA complex. To obtain Cu_2O nanocrystals, subsequently, the precursor solution was quickly heated to 160−220 °C and kept there for a certain period of

---

(56) Cotton, F. A.; Wilkinson, G. *Advanced Inorganic Chemistry*, 4th ed.; John Wiley & Sons: New York, 1980; Chapter 3, p 61.

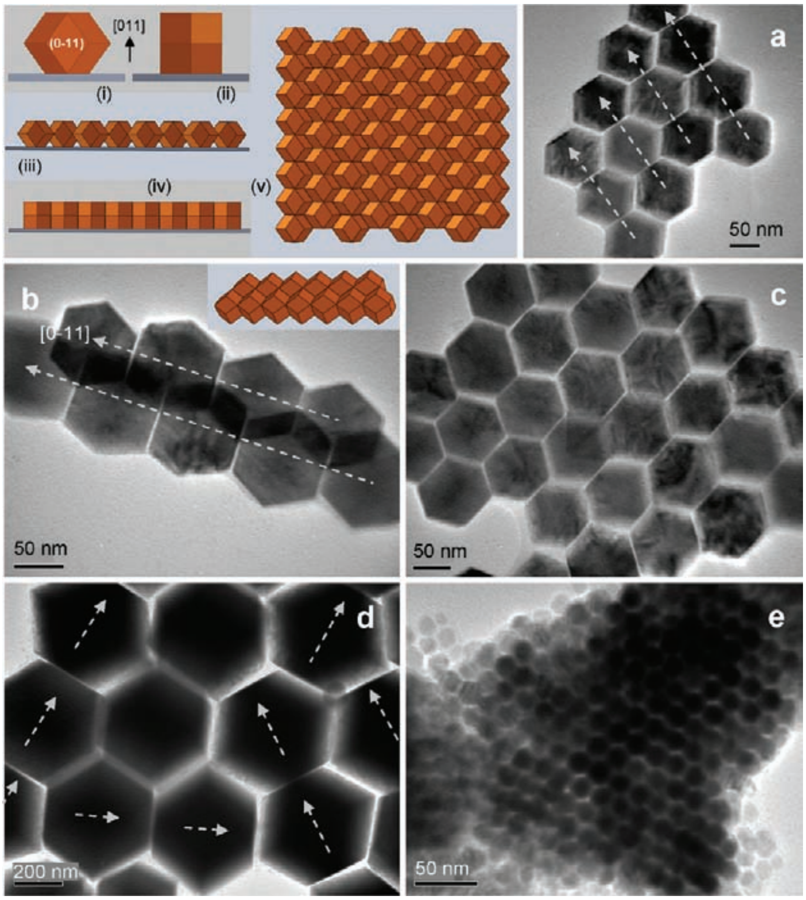

Figure 7. [011]-Oriented assemblies of Cu_2O rhombic dodecahedra (TEM images): (a) aligned along the [0−11] direction, (b) two overlapped [0−11] aligned rows (inset for a side view), (c) monolayer arrays, (d) randomly aligned dodecahedra, and (e) 3D superlattices; arrows indicate the [0−11] direction of the crystal. Color inset illustrates (i) side view along the [0−11] axis, (ii) side view along the [100] axis of a Cu_2O dodecahedron, (iii) side view along the [0−11] axis, (iv) side view along the [100] axis, and (v) top view along the [011] axis of a Cu_2O monolayer array.

time (see subsection 2.1). Afterward, Cu_2O products such as nanocubes could be separated from the solution by centrifugation. On the basis of these observations, the major process steps on the formation of Cu_2O nanocrystals are summarized in Figure 1. Besides as a chelating agent, HDA can also work as a reductant in our synthesis, as have been described in the literature that long-chain alkylamines show strong reducibility at elevated temperatures.[22,38,39] In our experiments with absence of HDA, for instance, $Cu(Ac)_2 \cdot H_2O$ and undecane alone do not produce anything after 1 h of thermal treatment at 200 °C. With a small amount of HDA (e.g., 1.0 mL of HDA and 19.0 mL of undecane) added to the same $Cu(Ac)_2 \cdot H_2O$ and undecane, a large quantity of Cu_2O particles with sizes around 500 nm could be precipitated out of solutions within just 15 min, though the product particles are nonuniform and polydisperse (SI-1, Supporting Information). Therefore, we note that HDA at such a low concentration can reduce divalent copper but cannot really facilitate controlled crystal growth. With a higher HDA concentration in synthesis, the regulating role of HDA becomes more pronounced, and products tend to grow with well-defined crystal morphology and uniform size distribution, as have reported in Figures 4−7. In general, increasing HDA concentration in precursor solutions leads a larger range of Cu_2O dodecahedron assembly (e.g., 6.0 mL of HDA and 14.0 mL of undecane; SI-2, Supporting Information). When the volume ratio of HDA to undecane reaches 1, the resultant size of Cu_2O rhombic dodecahedra decreases to 20 nm (SI-3, Supporting Information). Finally, when the ratio of HDA to undecane becomes infinity (i.e., undecane was absent in our synthesis), the rhombic dodecahedra of Cu_2O turn into cubic morphology (i.e., formation of nanocubes), which will be further discussed shortly. On the basis of the above findings, we understand that in addition to acting as a reducing agent, HDA can also stabilize desired crystallographic planes of building blocks and thus regulate the crystal growth of Cu_2O.

The rate of formation of Cu_2O building blocks is determined by reaction temperature. During the heating process, the precursor solutions turned into yellow-green color in the first 10 min at about 150 °C and then into yellow color in 30 min at 200 °C, noting that yellow is a color indicating the formation of nanostructured Cu_2O. Under our experimental setting, heating above 160 °C is essential for the formation of Cu_2O nanocubes, because no product is formed below this temperature. However, syntheses at higher temperatures (e.g., 220 °C) produce truncated nanocubes (SI-4, Supporting Information), possibly because the {001} family of crystal planes becomes more reactive when thermal desorption of HDA capping takes place at high temperatures. It is noteworthy that reaction temperature also governs the product composition. In this work, a relatively low temperature was taken to ensure a reduction just to monovalent copper (i.e., Cu_2O products) instead of metallic copper, which could be formed at 230 °C.[39] However, our Cu_2O products seem not to be too dependent on the concentration of copper precursor salt $Cu(Ac)_2 \cdot H_2O$. For example, Cu_2O nanocubes could be obtained at the concentration range of 0.02−0.05 g/mL (weight of $Cu(Ac)_2 \cdot H_2O$/volume of HDA, subsection 2.1), and a further

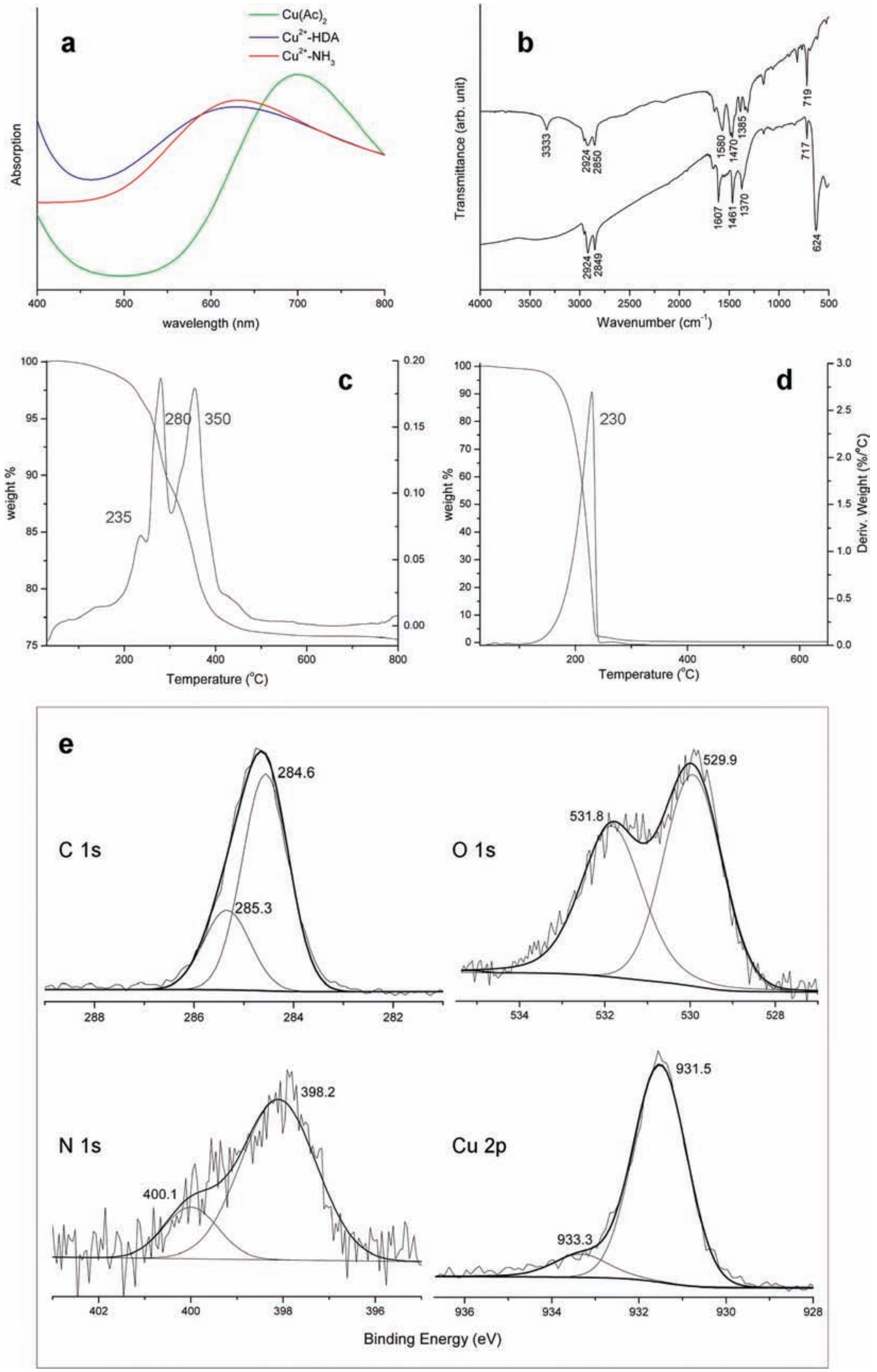

Figure 8. (a) UV−vis spectra for solution complexes, (b) FTIR spectra of the as-prepared Cu_2O nanocubes (lower) and as-received HDA sample (upper), (c) TGA/DrTGA curves for the as-prepared Cu_2O nanocubes, (d) TGA/DrTGA curves for the HDA sample, and (e) XPS spectra for the as-prepared Cu_2O nanocubes.

decrease in concentration produces relatively large Cu_2O disks, which can be easily stacked into 1D-assemblies (SI-5, Supporting Information), due to limited nucleation centers when the starting $Cu(Ac)_2 \cdot H_2O$ concentration is too low. Generally speaking, higher temperature and higher concentration of $Cu(Ac)_2 \cdot H_2O$ used in synthesis lead to larger Cu_2O products under a similar set of synthetic parameters (e.g., samples of Figure 7; SI-6, Supporting Information).

To elucidate formation of Cu_2O superlattice structures, several analytic techniques were further employed in sample characterization (subsection 2.4). First, the as-obtained samples were investigated with FTIR spectroscopy. As presented in Figure 8b, the absorption peak at 3333 cm^{-1} in the spectrum of HDA sample is assigned to asymmetric stretching mode of N−H bond.[57] However, it is hardly discernible at the same position in the spectrum of Cu_2O nanocubes, which is ascribed to a strong interaction between the alkylamine ends and monovalent copper ions on the surface.[57] Two peaks located at 2924 and 2849 cm^{-1} are assigned to asymmetric and symmetric stretching modes of CH_2, and the bands at 1607 and 717 cm^{-1} are attributed to deformation vibrations of alkylamines respectively (i.e., 1607 cm^{-1} to N−H scissor vibration and 717 cm^{-1} to N−H out-of-plane bending vibration).[57] Furthermore, absorption peaks of C−H asymmetric and symmetric deformation vibrations are located at 1461 and 1370 cm^{-1}, respectively, and the large absorption band at 624 cm^{-1} is assigned to copper−oxygen stretching vibration in the Cu_2O phase. A weak shoulder band located between 1607 and 1461 cm^{-1} peaks is attributable to stretching vibration of nitroso group (N=O; due to oxidation under ambient conditions) in aliphatic compounds that normally appears in ∼1550 cm^{-1}. All of these IR absorptions indicate that the alkylamines are anchored on the surfaces of Cu_2O nanocrystals. In order to quantify the amount of HDA in the Cu_2O supercrystals, TGA was used in this compositional determination. For example, Figure 8c shows that Cu_2O nanocubes have a ∼24.5 wt % decrease in weight from 75 to 800 °C. The weight loss at 235 °C belongs to the evaporation of HDA, and the weight loss at 280 °C to a comprehensive result of Cu_2O reduction to copper metal and the HDA evaporation. The assignment of evaporation of HDA was also confirmed with TGA, which indeed shows a weight loss at ∼230 °C (Figure 8d). Consistent with the report data in the literature,[32] a further increase in temperature to ∼350 °C results in HDA decomposition in the presence of Cu/Cu_2O catalysts, since the samples after this TGA analysis were proven to be a mixture of Cu_2O and metallic copper (XRD result; SI-7, Supporting Information). Thus it is calculated that there is ∼15−24.5 wt % of HDA in our assembled Cu_2O nanocubes, assuming all of the HDA-capped Cu_2O is reduced to pure metallic copper and is kept as pure Cu_2O, respectively. In order to further understand chemical interaction between the Cu_2O and HDA capping molecules, surface sensitive technique XPS was also applied in the present work. As shown in Figure 8e, the C 1s photoelectron spectrum can be deconvoluted into two peaks at 284.6 and 285.3 eV, and these two peaks are assigned to, respectively, adventitious hydrocarbon and the carbon atoms bonding with nitrogen of amine groups.[58,59] In the N 1s photoelectron spectrum, the main peak located at 398.2 eV belongs to C-NH_2 of HDA,[59,60] which reveals that the majority of adsorbed HDA remains chemically stable. Consistent with the FTIR finding, the small N 1s peak at around 400.1 eV can be attributed to presences of nitroso group (N=O) and amide group (O=C−NH_2) which normally fall in the range of 396−402 eV due to a small degree of surface oxidation under ambient conditions.[61−64] In the O 1s photoelectron spectrum, the peaks located at 529.9 and 531.8 eV are clearly attributable to the lattice oxygen of Cu_2O and to the oxygen species of surface hydroxyl/nitroso groups, respectively.[65] Finally, the two peaks at 931.5 and 933.3 eV in the Cu 2p photoelectron spectrum should arise from Cu_2O in the surface region and ambient-oxidized Cu^+ (i.e., Cu^{2+}) surface species.

According to the above analyses, the formation mechanism of the Cu_2O superlattice structure can be further addressed. Initially, HDA as a phase-transfer agent introduces inorganic salt into the organic phase. Our controlled experiments show that copper acetate hardly dissolves in undecane without HDA, even at a temperature as high as 200 °C. Afterward, HDA serves as a reducing agent for the formation of Cu_2O phase. Divalent copper ions in the present work can be reduced to monovalent copper ions without protection of inert gas. Different from the literature reports that organic amines exhibit a strong reducibility within inert atmosphere at elevated temperatures,[4,39] our ambient synthetic conditions retard the reducibility of HDA and make it become a moderate reductant more suitable for Cu_2O formation, noting that both nitroso and amide groups have been observed by FTIR (Figure 8b) and XPS (Figure 8e) methods. Finally, HDA regulates Cu_2O morphological growth and their self-assembly by absorbing on the metal cations of the Cu_2O nanocrystals. At low concentrations, HDA prefers to stabilize the facets of {110}, producing uniform dodecahedrons with ∼100% yield. At higher concentrations, on the other hand, HDA turns to stabilize the facets of the {001} family, leading to formation of cubic morphology (also a 100% yield). This change may be attributable to the difference in HDA adsorption on the two types of crystal facets, which have different geometric structures and atomic ratios of Cu/O. For instance, because these passivated crystal facets were formed during the synthesis, copper cation terminated surfaces (color illustrations, Figure 1) are likely formed as a result of the strong nucleophilic nature of alkylamines. Since the Cu^+ cation density on the {001} and {110} is 11.0 and 7.8 atoms/nm^2, respectively, high concentration of HDA obviously favors more adsorption of HDA on the copper-terminated the {001} facets, which stabilizes cubic morphology. As evidenced in the XRD patterns of Figure 2a, the formation rate of Cu_2O nanocubes is much slower, compared with their dodecahedral counterpart (see the patterns after 0.5 h of reaction). Because they are passivated with HDA surface capping, the average size of the grown Cu_2O nanocubes is only about 10 nm (9.1 ± 0.6 nm to be exact, as discussed earlier) after 1.5 h of reaction at 200 °C (Figure 3a,b,d−f; the reaction time in Figure 3c is 1 h), whereas the Cu_2O rhombic dodecahedra have an average size of about 70 nm at the same reaction temperature but with an even shorter reaction time (200 °C and 1 h; Figure 7a−c and SI-6 in Supporting Information). One interesting observation is that the octahedrons faceted with the {111} crystal planes were not observed in our Cu_2O products. The relative reactivity of copper ions in different Cu_2O crystal planes apparently may depend on a number of process factors,

---

(57) Meulenberg, R. W.; Strouse, G. F. *J. Phys. Chem. B* **2001**, *105*, 7438–7445, and references therein.
(58) Yao, K. X.; Zeng, H. C. *J. Phys. Chem. C* **2007**, *111*, 13301–13308.
(59) Lindberg, B.; Maripuu, R.; Siegbahn, K.; Larsson, R.; Golander, C. G.; Eriksson, J. C. *J. Colloid Interface Sci.* **1983**, *95*, 308–321.
(60) Borchert, H.; Talapin, D. V.; McGinley, C.; Adam, S.; Lobo, A.; de Castro, A. R. B.; Moller, T.; Weller, H. *J. Chem. Phys.* **2003**, *119*, 1800–1807.
(61) Batich, C. D.; Donald, D. S. *J. Am. Chem. Soc.* **1984**, *106*, 2758–2761.
(62) Nowak, A. M.; McCreery, R. L. *Anal. Chem.* **2004**, *76*, 1089–1097.
(63) Strobel, M.; Sullivan, N.; Branch, M. C.; Park, J.; Ulsh, M.; Kapaun, R. S.; Leys, B. *J. Adhes. Sci. Technol.* **2000**, *14*, 1243–1264.
(64) Kishi, K.; Chinomi, K.; Inoue, Y.; Ikeda, S. *J. Catal.* **1979**, *60*, 228–240.
(65) Xu, R.; Zeng, H. C. *Langmuir* **2004**, *20*, 9780–9790.

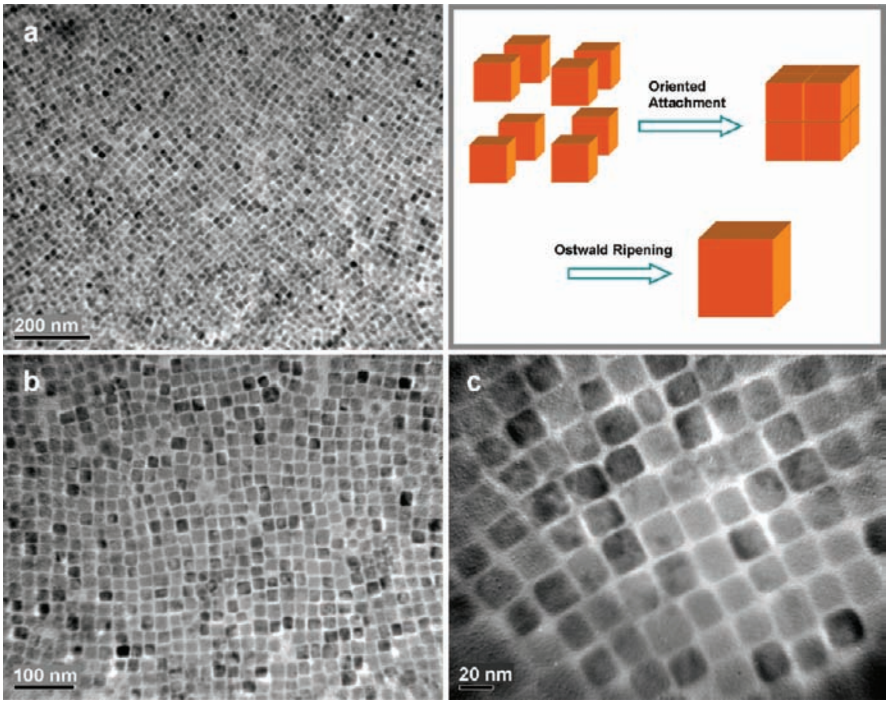

Figure 9. Disassembly and reassembly of Cu_2O nanocubes (a−c, TEM images different magnifications). During the disassembly of Cu_2O supercrystals via refluxing (60 min, subsection 2.2), the primitive nanocubes have undergone a size-doubling growth. The final nanocubic crystals were reassembled through a slow evaporation process described in subsection 2.2. Color inset illustrates a "2 × 2 × 2" oriented attachment with an Ostwald ripening process responsible for the observed crystal growth.

such as degree of unsaturated bonding ability of copper ions, surface anion and cationic density, geometric restrictions of active sites (including possible HDA-induced surface reconstruction), molecular size hindrance of adsorbates, concentration of adsorbing species (e.g., HDA), and of course the reaction temperature, etc. used in the synthesis. Future experimental work and theoretical calculation may help to address these issues further.

3.3. Disassembly and Reassembly of Superlattices. Because Cu_2O nanocrystals are self-assembled together through van der Waals interaction among the surface HDA molecules, it is conceivable that the assembled superlattices can be disassembled once the number of HDA is reduced and vice versa. To test this idea, we carried out a range of disassembly reassembly experiments using toluene as a solvent to partially remove HDA surfactants from the crystal surfaces. In Figure 9, for example, single layer arrays of squarely reassembled Cu_2O nanocubes can be obtained from their 3D supercrystals through reflux and a slow evaporation process described in subsection 2.2. Quite interestingly, after this disassembly process, most of the nanocubes in Figure 10 have increased their cube sizes to ∼20 nm. To explain this, oriented attachment among the nanobuilding blocks is thought as an underlying mechanism responsible for the observed size enlargement. Understandably, the peripheral nanocubes should first fall off larger supercrystal aggregates and some of the adsorbed HDA molecules are readily removed during the reflux process. Without an adequate protection of surfactants, Cu_2O nanocubes would tend to join together through "oriented attachment".[66−69] The color inset of Figure 9 illustrates a so-called "2 × 2 × 2" process in which each nanobuilding block of Cu_2O was attached to a neighbor in all three directions. Consistent with this model, Figure 10a−c reveals that different modes of attachments have taken placed during the disassembly processes and the resultant products are separated into domains according to their sizes (18.4 ± 1.7 nm: "2 × 2 × 2" process, Figure 10a,b; 28.7 ± 2.8 nm: "3 × 3 × 3" process, Figure 10a,c), although other higher orders of attachments (i.e., some larger cubes) can still be seen within the domains. Since the sizes of the newly formed cubes are multiples of that of pristine ones (9−10 nm, Figure 2), the oriented attachment becomes plausibly a primary mechanism for the observed crystal growth. However, other processes such as Ostwald ripening are also operative since there is no intercube gaps observed in the resultant cubes. Consistent with this mechanism, the Cu_2O rhombic dodecahedral building blocks also show similar aggregative crystal growth under refluxing conditions. Since there are less adsorbed HDA molecules on the {110}-type surfaces, the attachment among the rhombic dodecahedral building blocks is expected to proceed more completely. Indeed, no freestanding nanobuilding blocks of this type can be found in the refluxed products, as reported in Figure 10d−f. It should also be pointed out that, different from those presented in Figures 4−7, the rhombic dodecahedra of Cu_2O in Figure 10d−f have been atomically fused after going through oriented attachment despite rather similar TEM images.

3.4. Sensing Applications of Self-Assembled Superlattices. As a *p*-type semiconductor, nanostructured Cu_2O has been investigated for its gas sensing applications, including ethanol sensing with unorganized single-crystalline spheres (∼220 nm), microspheres, and microarchitectures of Cu_2O.[31,35,36] In view of the lack of investigations with organized nanostructured Cu_2O, we will examine herein the effects of our smaller self-assembled Cu_2O nanocubes in ethanol sensing application. Figure 11a

---

(66) Penn, R. L.; Banfield, J. F. *Science* **1998**, *281*, 969–971.
(67) Pacholski, C.; Kornowski, A.; Weller, H. *Angew. Chem., Int. Ed.* **2002**, *41*, 1188–1191.
(68) Liu, B.; Zeng, H. C. *J. Am. Chem. Soc.* **2003**, *125*, 4430–4431.
(69) Penn, R. L. *J. Phys. Chem. B* **2004**, *108*, 12707–12712.

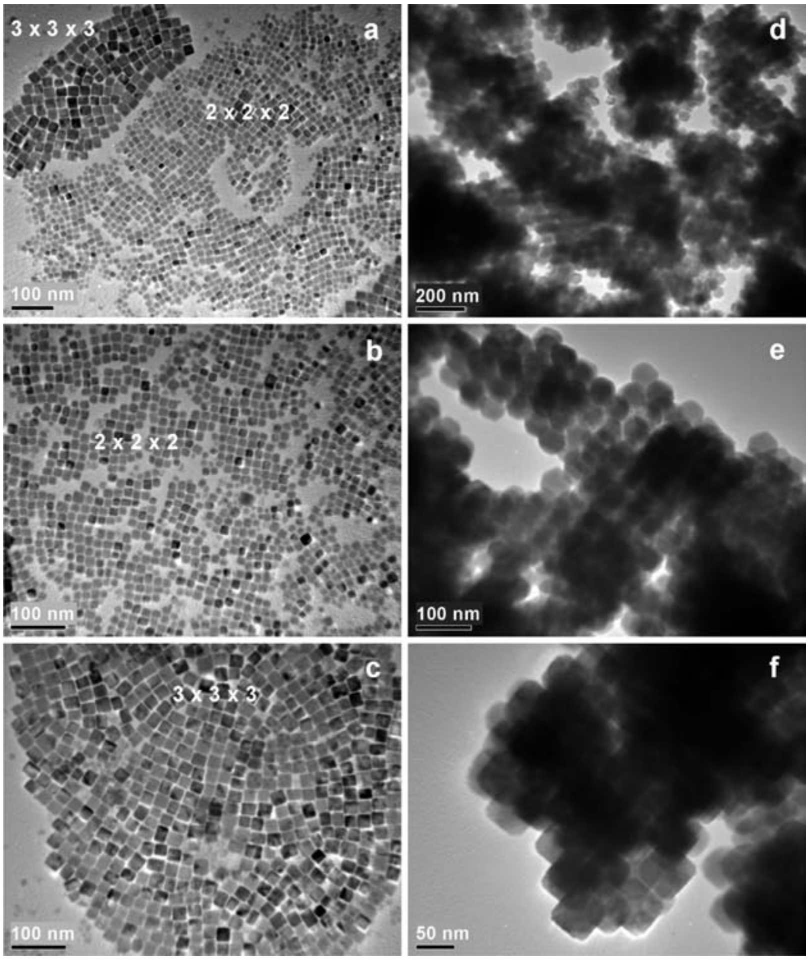

Figure 10. Disassembly of Cu_2O supercrystals after a reflux treatment (subsection 2.2) for 60 min (TEM images): (a) two different types of domains can be seen in the same sample, (b) a "2 × 2 × 2" dominating 2D aggregate, and (c) a "3 × 3 × 3" dominating 2D aggregate. Formation of 3D aggregates of Cu_2O dodecahedra (d−f, TEM images) after the same reflux treatment for 60 min.

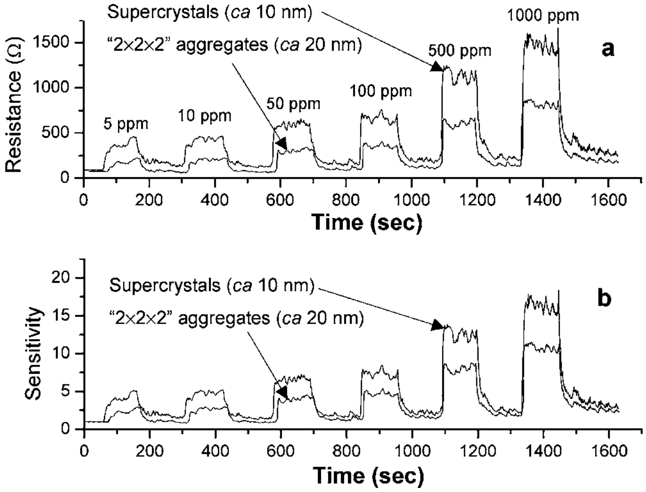

Figure 11. (a) Gas (ethanol) sensing performances at 150 °C and (b) their related sensitivities ($S = R_G/R_A$) using supercrystals of Cu_2O nanocubes and the "2 × 2 × 2" dominating aggregates, respectively, in sensor fabrications. Note that the initial Cu_2O nanocube sizes are approximately 10 and 20 nm in the above two cases, and the measurements were conducted under identical conditions.

compares two types of Cu_2O nanocubes used under identical sensing conditions (see subsection 2.3). The precursor slurries used for sensors were prepared from self-assembled 3D superlattices and reflux treated (disassembled) nanocubes (i.e., about 10 and 20 nm in size, respectively). Although both types of Cu_2O can provide very good sensing capability, the organized Cu_2O is apparently even better. The operating principles of *p*-type transition metal oxide chemiresistor gas sensors are based on change of sensor conductivity by controlling mobile charge carriers. Without target analytes, molecular oxygen from air ambience will adsorb on the surface defects of the metal oxides, forming some negatively charged ions O^-, O_2^-, and O^{2-}. Compared to *n*-type transition metal oxides, however, fewer anionic oxygen species can be formed on the *p*-type transition metal oxides because of their lower surface electron density.[53] Nevertheless, the presence of the anionic oxygen species acts as a negatively applied quasi-gate voltage and results in a localized accumulation of holes near the surfaces of *p*-type metal oxides. The consumption of electrons and thus the presence of this quasi-gate voltage lead to a better separation of the holes from electrons, and an operating sensor of this type has a low resistance in the absence of reducible gaseous analytes. When the *p*-type Cu_2O is exposed to ethanol/air mixtures, in the present case, electrons from the redox reactions between ethanol and adsorbed surface oxygen will be injected to the conduction band of Cu_2O and the recombination between the electrons and holes will result in a lower carrier concentration. Understandably, decrease in the number of surface oxygen species through redox reactions implies reducing the magnitude of the negative quasi-

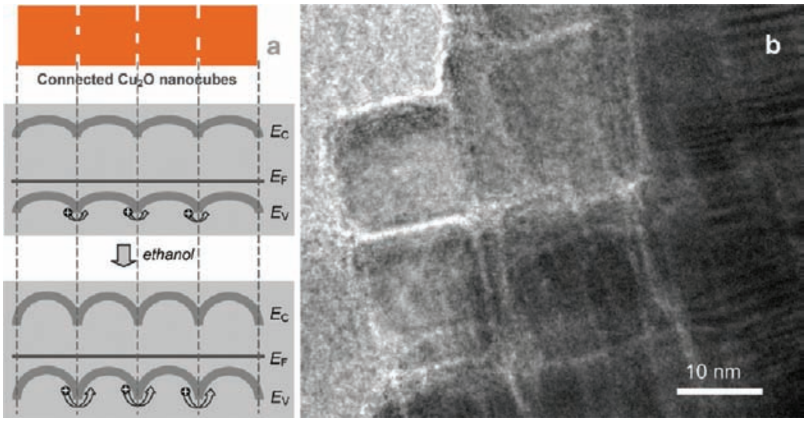

Figure 12. (a) Simplified schematic energy diagrams of a 1D array of Cu_2O nanocubes upon the ethanol sensing, where E_F, E_V, and E_C are Fermi energy, valence band energy, and conduction band energy, respectively, and hole carriers are represented by positive signs. (b) HRTEM image for the 200 °C treated supercrystals of Cu_2O nanocubes.

gate voltage, which in turn increases the resistance of Cu_2O. As expected, in Figure 11a the resistance indeed significantly increases at the moment the sensor is exposed to the ethanol/air mixture. Moreover, the sensors also own quick response/recovery time and high sensitivity at a relatively low working temperature of 150 °C (Figure 11b), even compared with *n*-type oxide sensors such as SnO_2 and In_2O_3.[70,71] Apart from carrier population control, contact potential barrier between metal oxide particles is another important factor that affects the resistivity of this type of gas sensors. The significant variation in resistance observed in Figure 11a for the organized Cu_2O nanocubes can be attributed to small sized crystallites in the sensor, which has a high surface to bulk ratio and thus a greater carrier depletion layer when exposed to reducing analytes. This postulation is further supported with our HRTEM investigation in Figure 12. It is convincing to note that the original cubic organizations of nanobuilding blocks observed in Figure 2 are still well preserved after the heat-treatment (Figure 12b). However, the intercube distance is apparently shortened since a certain contact among the nanocubes has been generated after thermal removal of HDA at 200 °C (subsection 2.3). As the overall structure of nanocubic organization is essentially not altered, it is believed that there must be a global crystallographic relationship among the connected nanocubes, which may account for the low resistances observed in our sensors. Indeed, the baseline recorded in Figure 11a for the organized nanocubes is quite close to that of the reflux-treated sample, despite a significantly higher density of contacts present in the former case. Synergistically, a greater carrier depletion layer and a relatively small contact potential would lead to a significant sensitivity enhancement in the case of our organized nanocubes, as illustrated schematically in Figure 12a. It should also be mentioned that the sensors prepared from our orderly organized Cu_2O nanocubes have shown a lower detection limit (5 ppm), a lower operating temperature (150 °C), and higher sensitivities (Figure 11b) for ethanol vapor sensing, compared with some reported works using Cu_2O in the recent literature.[31,35,36] Another important feature for the above-reported Cu_2O nanocube sensors is low sensor resistances,[35] which correspondingly requires low resistant coupling resistors, that is, impedance matching with amplifying circuits can be easily achieved leading to less manufacturing cost for device fabrication.[72]

4. Conclusions

In summary, using copper(II) alkylamine (1-hexadecylamine; HDA) complex as a starting precursor, two types of monodisperse unifaceted nanobuilding blocks (cubic or dodecahedral) with sizes small than 100 nm have been successfully synthesized at 200 °C under atmospheric pressure. In this approach, HDA plays a number of important roles for the formation of Cu_2O supercrystals and superstructures: it serves as a chelating agent to form $[Cu(NH_2C_{16}H_{33})_4]^{2+}$ complex, as a phase-transfer agent to convey Cu^{2+} precursor into the organic phase, as a reductant to change divalent copper ions to monovalent ones, as a growth regulator to control crystal morphology, and as a capping surfactant on crystal facets to generate self-assemblies of nanocrystals via van der Waals interaction. Because of their uniform size and faceted crystal morphology, these nanocrystals can be further assembled into supercrystals and superstructures. With cubic building units, supercrystals of Cu_2O are arranged solely according to a simple cubic crystal system with the [001] orientation toward the surface normal. With rhombic dodecahedral crystals, four types of superlattices of Cu_2O with different surface orientations can be obtained (i.e., along the [112], [111], [001] and [011] directions) depending on a balance between crystal-support interaction and mutual engagement among the crystal building units. By refluxing as-synthesized Cu_2O products in toluene solvent, self-assembled Cu_2O nanocubes in the supercrystals can be disassembled and enlarged owing to partial removal of their surface alkyamine that allows an aggregative crystal growth via both “oriented attachment” and Ostwald ripening processes. Due to the presence of relatively active crystal planes, however, the Cu_2O rhombic dodecahedra in their superlattices are fused into pseudosingle-crystals because of “oriented attachment” taking place among these crystal building units under the same reflux treatment. Through a slow evaporation process, on the other hand, the disassembled Cu_2O nanocubes can be reassembled into monolayer superlattices. The investigation for ethanol vapor detection has concluded that the orderly arranged Cu_2O nanocubes exhibit advantages in sensing

---

(70) Azad, A. M.; Akbar, S. A.; Mhaisalkar, S. G.; Birkefeld, L. D.; Goto, K. S. *J. Electrochem. Soc.* **1992**, *139*, 3690–3704.

(71) Eranna, G.; Joshi, B. C.; Runthala, D. P.; Gupta, R. P. *Crit. Rev. Solid State Mater. Sci.* **2004**, *29*, 111–188.

(72) Liang, Y. X.; Chen, Y. J.; Wang, T. H. *Appl. Phys. Lett.* **2004**, *85*, 666–668.

performance and device fabrication, compared with other Cu_2O-based alcohol sensors recently reported in the literature.

Acknowledgment. The authors gratefully acknowledge the financial support provided by National University of Singapore, Economic Development Board, Singapore, and King Abdullah University of Science and Technology, Saudi Arabia.

Supporting Information Available: Synthetic parameters, TEM images, and XRD pattern. This material is available free of charge via the Internet at http://pubs.acs.org.

JA100151F